Applied Thermal Engineering 246 (2024) 122873

Contents lists available at ScienceDirect

Applied Thermal Engineering

journal homepage: www.elsevier.com/locate/apthermeng

Research Paper

Impacts of distributed thermal and electric contact resistance on performance and geometric optimization of thermoelectric generators

Ying Li [a,b], Yong Shi [a,*], Ding Luo [c], Xuehui Wang [d], Yuying Yan [b,*]

[a] Department of Mechanical, Materials and Manufacturing Engineering, University of Nottingham Ningbo China, Ningbo 315100, China
[b] Fluids and Thermal Engineering Research Group, Faculty of Engineering, University of Nottingham, Nottingham NG7 2RD, UK
[c] Department of Engineering Mechanics, Key Laboratory for Thermal Science and Power Engineering of Ministry of Education, Tsinghua University, Beijing 100084, China
[d] School of Mechanical and Materials Engineering, University College Dublin, D04 V1W8 Dublin, Ireland

ARTICLE INFO

Keywords:
Thermoelectric generator
Distributed thermal contact resistance
Distributed electric contact resistance
Performance assessment
Geometric optimization

ABSTRACT

Thermal and electric contact resistance (TCR/ECR) critically impact performance and geometric optimization of thermoelectric generators (TEGs). However, conventional treatments usually ignored or simplified them as lumped variables, neglecting their actual distributions across the TEG system. In this study, we proposed a multi-physical model to characterize TEG performance with explicitly specifying TCRs/ECRs at different TEG interfaces (locations). The numerical results show that the lumped-variabletreatment led to maximal overestimations of 16.9 % and 24.5 % in the TEG output power and efficiency, respectively, compared to the results with distributed TCR in this article. Importantly, it also reveals that the TEG performance was susceptible to the TCR location—the interfaces on the cold side exerted more negative impacts than those on the hot side. Furthermore, reducing both TCR and ECR could improve TEG performance and reducing TCR is more effective. It is shown that an 80 % reduction in TCR increased the maximum TEG output power by 35.6 %, while the same reduction percentage in ECR only improved it by 8.8 %. As to geometric optimization, an optimal TE leg height equal to 0.6 mm was obtained for the maximum output power. This contrasts with previous studies without considering TCR and ECR, which always favoured shorter heights. As for copper electrodes, their optimal heights were in the range of 0.2–0.4 mm corresponding to the maximum efficiency, far smaller than those (0.7–1.2 mm) obtained when TCR/ECR were neglected. The latter even further resulted in a reduction in the maximum efficiency by more than 1 % compared to its true peak. In this study, all these numerical results clearly elucidate the important impacts of distributed TCR and ECR on TEG performance, and provide a comprehensive and balanced guideline for TEG design.

1. Introduction

Thermoelectric generator (TEG) has become a research hot spot in recent years due to its distinct advantages of no pollution, no moving parts, no noise, and a long lifespan [1]. As a promising energy conversion device, its application has been widely explored in various areas, including body heat harvest [2–4], natural heat energy capture [5–10], industrial waste heat recovery [11–14], and household waste heat harvest [15–17].

The performance of a TEG is characterized by its maximum output power, P_{max}, and maximum efficiency, η_{max}.When the parasitic thermal and electric losses are considered, these performance indicators are expressed by the TEG effective dimensionless figure of merit, $Z_{eff}\overline{T}$, the temperature difference upon TE legs, ΔT_l, and the TEG electric resistance, R_{TEG}, as shown by [18],

$$P_{max} = \frac{(\alpha \Delta T_l)^2}{4(R_{TEG})} = \frac{(\alpha \Delta T_l)^2}{4(R_i + R_{ipara})}, \tag{1}$$

$$\eta_{\max} = \frac{\sqrt{1 + Z_{eff}\overline{T}} - 1}{\left(\sqrt{1 + Z_{eff}\overline{T}} + T_{cl}/T_{hl}\right)} \frac{\Delta T_l}{T_{hl}}, \tag{2}$$

where R_{TEG} is further decomposed into R_i and R_{ipara}. In Eq. (2), $Z_{eff}\overline{T}$ can be specified by [18],

* Corresponding authors.
E-mail addresses: Yong.Shi@nottingham.edu.cn (Y. Shi), Yuying.Yan@nottingham.ac.uk (Y. Yan).

https://doi.org/10.1016/j.applthermaleng.2024.122873
Received 17 November 2023; Received in revised form 1 March 2024; Accepted 3 March 2024
Available online 5 March 2024

Nomenclature

Symbols

A_h	cross sectional area of hot-side ceramic (m^2)
E	intensity of electric field (V)
h_c	copper electrode height (mm)
h_c^o	optimal copper electrode height for maximum output power (mm)
h_c^{oo}	optimal copper electrode height for maximum efficiency (mm)
h_l	TE leg height (mm)
h_l^o	optimal TE leg height for maximum output power (mm)
h_l^{oo}	optimal TE leg height for maximum efficiency (mm)
j	electric current (A)
K	thermal conductance of TEG (W/K)
P	output power (W)
q	magnitude of heat flux (W/m^2)
q	input heat flux (W/m^2)
Q	internal heat source (W)
R_e	external load resistance (Ω)
R_e^o	optimal external load resistance for maximum output power (Ω)
R_e^{oo}	optimal external load resistance for maximum efficiency (Ω)
R_E	electric contact resistance ($\Omega\bullet m^2$)
R_{TEG}	electric resistance of TEG (Ω)
R_i	electric resistance of TE legs (Ω)
R_{ipara}	parasitic electric resistance in TEG (Ω)
R_T	thermal contact resistance ($m^2\bullet K/W$)
T	temperature (K)
ΔT_l	temperature difference upon TE legs (K)
V	output voltage (V)
U	electric potential (V)

Greek symbols

α	Seebeck coefficient (V/K)
η	conversion efficiency (%)
λ	thermal conductivity (W/m^2 K)
ρ	electric resistivity (Ω m)

Acronyms

ECR	electric contact resistance ($\Omega\bullet m^2$)
TCR	thermal contact resistance ($m^2\bullet K/W$)
TE	thermoelectric
TEG	thermoelectric generator
$Z_{eff}\overline{T}$	effective dimensionless figure of merit of TEG
$Z\overline{T}$	dimensionless figure of merit of TE material

Subscripts

c	cold side
cl	cold side of TE legs
co	copper electrode
ce	ceramic
dis	with distributed TCR and ECR
exc	external cold-side
exh	external hot-side
h	hot side
hl	hot side of TE legs
inc	internal cold-side
inh	internal hot-side
i	*i* components
l	TE legs
max	maximum
n	n-type TE legs
p	p-type TE legs

$$Z_{eff}\overline{T} = \frac{\alpha^2}{K\cdot R_{TEG}}\overline{T} = \frac{\alpha^2}{K\cdot\left(R_i + R_{ipara}\right)}\overline{T}. \tag{3}$$

Based on Eqs. (1)−(3), it is seen that a larger ΔT_l, smaller R_i and R_{ipara} will contribute to better TEG performance.

We point out that for a TEG system, its thermal and electric contact resistance (TCR and ECR) exert significant impacts on its performance. To be specific, a larger TCR and ECR will lead to a lower ΔT_l and a higher R_i, respectively, both of which essentially degrade TEG performance [19–24]. Even worse, such degradation will become more significant with the decrease of TE leg heights. Unfortunately, this intrinsic link has been completely ignored by a number of previous works, which, for simplicity, evaluated TEG performance and optimized its geometry without considering TCR and ECR at all [25–33]. For example, Ref. [32] investigated an asymmetrical annular TEG and Ref. [33] optimized a segmented annular TEG. Both studies focused on the improvement of TEG performance; however, neither of them accounted for the TCR and ECR at the interfaces in their respective TEG systems. Critically, the crude treatment of neglecting TCR and ECR has led to various overestimations in TEG performance. Tan *et al.* [34] compared the output power and efficiency of an annular TEG with and without considering TCR and ECR. They revealed that the latter has overestimated the TEG output power and efficiency by up to 42.57% as compared to the former. Kim [35] even pointed out that when the TEGs used short TE legs, such an overestimation due to ignoring TCR and ECR could jump to 90%. It is evident that simply ignoring TCR and ECR did bring large errors, and misled the evaluation of TEG performance.

Over recent years more and more studies have recognized this issue and made efforts to correct the aforementioned misestimations. Among them one of the most common modifications is to introduce TCR and/or ECR as non-zero constant lumped variables [21,24,35,36]. For instance, Yao *et al.* [37] directly incorporated the TCR and ECR at the copper electrode/TE leg interfaces as lumped coefficients in their design and performance assessment of a photovoltaic-thermoelectric system. Wang *et al.* [38] treated the TCRs in their TEG experiments as the overall lumped variables at the heat source/ceramic and heat sink/ceramic interfaces, and found the TEG's maximum output power and efficiency have increased by 33% and 20%, respectively, with the decreasing lumped TCRs. Yusuf *et al.* [24] developed a genetic algorithm to optimise the TEG geometry with the lumped TCR and ECR. They revealed significant decreases in both the TEG output power and efficiency with an increase in the lumped ECR, while the corresponding lumped TCR had little effect. More layers of a segmented TEG with the lumped TCR and ECR were also studied by Zhao *et al.* [39] through use of a machine learning approach. It is shown that the former contact resistance significantly impacted the TEG output voltage, while the TEG output power and efficiency depended more heavily on the latter.

Note that not all the previous studies in the TEG literature reduced TCR and ECR as lumped variables. Some analytical and numerical studies showed strong interests in the TCR and/or ECR at some particular interfaces. To facilitate our following discussion, we classify the TCRs at different interfaces across a TEG system into the external hot-side TCR (at the heat source/ceramic interface), external cold-side TCR (at the heat sink/ceramic interface), internal hot-side TCR (consisting of the TCRs at ceramic/copper electrode and copper electrode/TE leg interfaces close to the heat source), and internal cold-side TCR (consisting of the TCRs at ceramic/copper electrode and copper electrode/TE leg interfaces close to the heat sink) [40,41]. In Ref. [42],

Zhang *et al.* analytically studied the influence of both the internal hot- and cold-side TCRs on TEG performance. Their results demonstrated the diminishing effect on the TEG performance associated with those decreasing internal TCRs. Kim [35] used a 2D numerical model to characterize the impact of the internal hot-side TCR specifically at the copper electrode/TE leg interface. The simulations showed that a smaller internal hot-side TCR led to higher TEG output power. Ref. [43] delved into a segmented TEG and studied its efficiency with and without the internal TCR at the interface of its segmented TE legs. It was revealed that an increase by 20% in such a TCR led to a reduction by more than 20% in the TEG efficiency, compared to its TEG counterpart without considering the TCR. Similar extensive studies were also conducted on the external TCRs (i.e., those at heat source/ceramic and heat sink/ceramic interfaces). Siouane *et al.* [23] proposed an analytical model with two constant external TCRs imposed at the heat source/ceramic and heat sink/ceramic interfaces, and they solved the model for the TEG output voltage and equivalent electric resistance under different thermal boundary conditions. Their results indicated that the TEG output power decreased with the increasing external TCRs. Zhang *et al.* [44] discussed the impact of the external TCR between the skin and the wearable TEG. In this reference, the temperature drop caused by the external TCR was negligibly small when the ratio of the contact thermal conductance to thermal conductance of the flexible substrate exceeded 0.2. On the other hand, for the ECR at the copper eletrode/ TE leg interfaces, its impacts on TEG performance also attracted considerable interests. Kim [35] numerically investigated the influence of this ECR on the TEG outpower. It is shown that an increase in the ECR directly resultes in a reduction in the TEG output power. Similar phenomena have also been observed by Zhang *et al.* [42]—the output power and efficiency of the annular TEG in their study gradually decreased with the increasing ECR. In Ref. [45], Zhu *et al.* applied their artificial neural network model to corroborate that the TEG output power and efficiency deteriorated with the rising ECR. In fact, the effects of ECR on TEG performance become more pronounced when TE leg heights decrease. For example, in some flexible film TEGs with very short TE legs, the ECR could reach up to 50% of the total electric resistance; its reduction could increase the power factor by approximately 40% [20]. It is worth mentioning that many other studies further explored the joint impacts of the ECR and TCR at the copper electrode/TE leg interfaces. For example, Zhang *et al.* [42] theoretically studied the performance of an annular TEG, and found that the larger values of ECR and TCR at the copper electrode/TE leg interfaces have always led to a degradation in the TEG performance. Bjørk [43] discussed the segmented TE legs, and showed that to ensure a 30 % improvement in the efficiency of the segmented structure, the ECR and TCR at the copper electrode/TE leg interfaces should be less than 20% and 30% of the total electric and thermal resistances, respectively.

So far, all these previous studies have well examined the impacts of TCR and/or ECR on TEG performance. However, it is noted that they either treated TCR and/or ECR as lumped variables pertinent to the entire TEG system or were only interested in the specific TCR and/or ECR at the given locations. They lacked a full picture of TCRs and ECRs distributed at different interfaces across the TEG system, and failed to analyze the impacts of their locations on TEG performance [40,41]. From the practical point of view, each local TCR affects the temperature drop across the corresponding interface, while the ECR influences the Joule heat. Therefore, a good knowledge of those distributed TCRs and ECRs is of importance for specifying ΔT_l upon TE legs, thereby more reasonably assessing TEG performance. In this sense, the treatment of TCR and/or ECR as lumped variables is far from sufficient to reveal those interfacial effects; the studies on the TCR and/or ECR at a particular interface cannot describe the joint roles of contact resistances at different locations.

Besides the direct impacts on TEG performance as discussed above, TCR and ECR also play an important role in optimization of TEG structure. Kim *et al.* [35] demonstrated the inclusion of the TCR and ECR at copper electrode/TE leg interfaces led to an optimal TE leg height of 0.6 mm, completely different from the case ignoring the TCR and ECR. The latter always prefers a smaller TE leg height. Zhang *et al.* [21,42] and Tan *et al.* [34] studied the geometric optimization of annular TEG legs taking into account the TCR at ceramic/copper electrode and copper electrode/TE leg interfaces and ECR at copper electrode/TE leg interfaces. Similar findings were reported—When the TCR and ECR were taken into account, the smaller annular shape parameter derived by ignoring them was no longer regarded as the optimal shape parameter for annular TEG legs. In these studies, it was demonstrated that the optimal annular shape parameter gradually decreased with the decreasing TCR and ECR [21,42]. Zhao *et al.* [39] employed the machine learning method to investigate the influence of the TCR and ECR at interfaces between different segments of TE legs on the material design of a 5-layered segmented TEG. They found that these contact resistances even determined the optimal material combinations. In Ref. [46], Pietrzyk *et al.* optimized a conventional π-shaped TE module for a refrigerator. They suggested that the optimum B-factor, a geometric parameter of TE leg, should vary by up to 20% with the changes of the ECR. In Ref. [36], He *et al.* investigated the geometric optimization of TE legs considering the overall lumped TCR while ignoring the ECR of the TEG. It should be pointed out that although these studies provided in-depth insights into TEG structure, they still either treated TCR and/or ECR as lumped variables or just focused on the TCR and/or ECR at specific interfaces. These treatments could result in errors in the local temperature distributions and the temperature differences upon TE legs, and may further lead to inaccurate or even incorrect TEG optimal structures. Moreover, the geometric optimization in these studies was only interested in TE legs. No recommendations were made for optimizing the copper electrodes in use. So far, a comprehensive optimal solution including the geometries of both TE legs and copper electrodes is lacking.

In this work, we therefore propose a multi-physical model considering the explicit assignment of local TCRs and ECRs at different interfaces across a TEG. The magnitudes of these distributed contact resistances are specified based on the real on-site experimental scenarios [41]. This multi-physical model also couples both thermal and electric fields, and includes all the thermoelectric effects (Seebeck effect, Peltier effect and Thomson effect). Through numerical simulations of the model, we analyze the impact of each local TCR location on TEG performance and identify the most influential TCR location in the corresponding performance assessment. We compare TEG performance with distributed TCR with that obtained using the conventional lumped-TCR simplification, and highlight their differences. To the best of our knowledge, these findings have never been reported in previous studies. Furthermore, both the individual and joint impacts of distributed TCR and ECR on TEG performance are discussed in detail. Geometric optimization of TE legs and copper electrodes is also elaborated. All of these numerical simulations will provide a clear and in-depth understanding of the impacts of distributed TCR and ECR on TEG performance and geometric optimization. It could facilitate future TEG analyses and designs more suitable for practical applications.

The rest of the article is organized as follows. A multi-physical model is introduced in Section 2. Section 3 conducts its mesh independence test, followed by the validation of the model using experimental results. Based on numerical simulations of the model, the TEG output power and efficiency with distributed TCR are compared to those with lumped TCR in Section 4. In this section, we also analyze the influence of each TCR location, and discuss the impacts of distributed TCR and/or ECR on both TEG performance and the heights of TE legs and copper electrodes. Finally, the conclusions are drawn in Section 5.

2. Multi-physical model for TEG

Fig. 1 shows the schematic of a TEG system, where TCRs and ECRs at various interfaces are illustrated (For clarity, each contact resistance is represented by a curved transparent surface in Fig. 1). To be specific, the

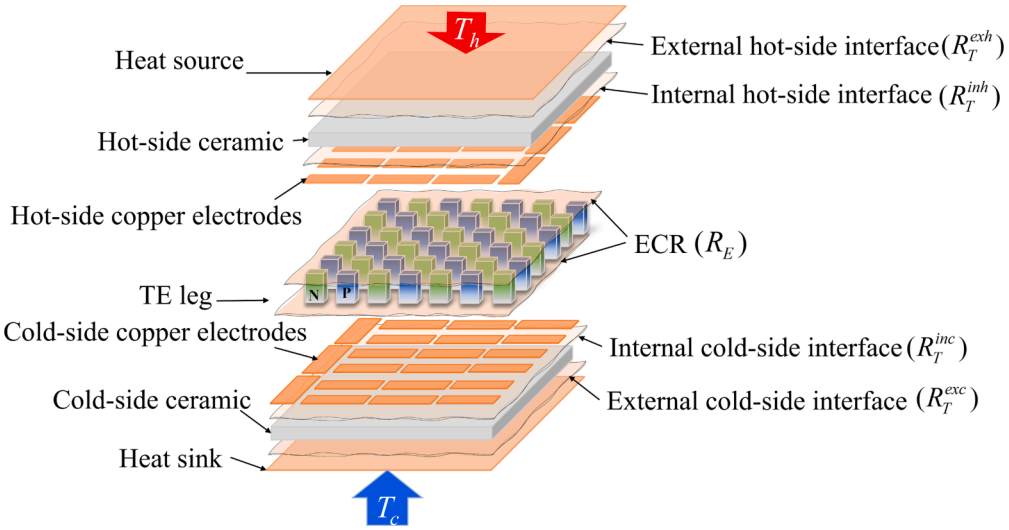

Fig. 1. Schematic of a TEG system and its TCRs and ECRs at different interfaces.

TCRs investigated in this article include the external hot-side TCR, R_T^{exh}, the external cold-side TCR, R_T^{exc}, the internal hot-side TCR, R_T^{inh}, and the internal cold-side TCR, R_T^{inc}. As to the ECRs, they are located at the hot- and cold-side copper electrode/TE leg interfaces. The magnitudes of the external TCRs and ECRs have been evaluated in our previous experimental study [41]. The overall thermal resistance from internal interfaces (including the ceramic/copper electrode and copper electrode/TE leg interfaces on both the hot and cold sides) was also obtained in these experiments [41]. In this numerical study, such an overall thermal resistance is evenly split into two parts, which are allocated to the ceramic/copper electrode interfaces on the hot and cold sides (i.e., the internal hot-side and cold-side interfaces as shown in Fig. 1), respectively. Each is then multiplied by the corresponding contact area, yielding R_T^{inh} and R_T^{inc}.

A multi-physical model with specifying those distributed TCRs and ECRs is proposed in this section. It integrates the Seebeck effect, Peltier effect and Thomson effect of TE materials, and uses the temperature-dependent material properties of TE legs. A fully-coupled solver characterizing the coupling thermal-electric effects in a TEG is employed to solve the numerical model. For simplicity, this model is established based on the following assumptions, namely

1) only the steady-state heat transfer is discussed;
2) the convective and radiative heat losses in the TEG are ignored;
3) the properties of ceramic layers and copper electrodes are treated as constants;
4) the top surface of the heat source and the bottom surface of the heat sink remain at two different constant temperatures, i.e., T_h and T_c ;
5) all the material properties are isotropic.

2.1. Governing equations

With the above assumptions, for a TEG operating at its steady state, its heat transfer and electric current are described by [47],

$$\nabla\cdot\boldsymbol{q} + Q = 0, \tag{4}$$

$$\nabla\cdot\boldsymbol{j} = 0. \tag{5}$$

In Eqs. (4) and (5), the variables in bold are the vectors. For ceramic substrates and copper electrodes, the corresponding governing equations have more specific forms, which are

$$\nabla\cdot(\lambda_{ce}\nabla T) = 0, \qquad \textit{for ceramic substrates}, \tag{6}$$

and

$$\nabla\cdot(\lambda_{co}\nabla T) + \boldsymbol{j}^2\rho_{co} = 0, \qquad \textit{for copper electrodes}. \tag{7}$$

As for TE legs, the heat transfer inside them involves the Seebeck effect, Peltier effect and Thomson effect. Its governing equations, therefore, consist of conductive heat, Joule heat, Peltier heat, and Thomson heat. It follows that.

$$\nabla\cdot\left(\lambda_p(T)\nabla T\right) + \boldsymbol{j}^2\rho_p(T) + \nabla\alpha_p(T)\cdot\boldsymbol{j}T + \frac{d\alpha_p(T)}{dT}T\boldsymbol{j}\cdot\nabla T = 0, \qquad p-\textit{type legs}, \tag{8}$$

$$\nabla\cdot\left(\lambda_n(T)\nabla T\right) + \boldsymbol{j}^2\rho_n(T) + \nabla\alpha_n(T)\cdot\boldsymbol{j}T + \frac{d\alpha_n(T)}{dT}T\boldsymbol{j}\cdot\nabla T = 0, \qquad n-\textit{type legs}. \tag{9}$$

Note that the electric field **E** in TE legs is subject to

$$\boldsymbol{E} = -\nabla U - \alpha_i(T)\nabla T, \qquad i = p \textit{ or } n, \tag{10}$$

and

$$\boldsymbol{j} = \frac{\boldsymbol{E}}{\rho_i}, \qquad i = p \textit{ or } n. \tag{11}$$

For convenience, all the material properties used in our simulation and the relevant geometric parameters of each component are summarized in Tables 1 and 2.

2.2. Numerical settings and boundary conditions

In this work, Eqs. (4)–(11) were solved by COMSOL using the finite element method (FEM). The computational domain and boundary conditions are shown in Fig. 2. Note that the heat source (heater and aluminium block) and heat sink (water loop block) in the experiment (as shown in Fig. 4) are not included; instead, they are replaced by two copper plates with a thickness of 0.1 mm at the temperatures of T_h and T_c. The reason for this simplification is because T_h and T_c have been directly measured in our experiments. They can thus be simply set as the top and bottom thermal boundary conditions. Furthermore, to form a closed circuit, an external load resistance, R_e, was introduced and electrically connected with two copper electrodes of the TEG. In the simulation, the TCRs at the four interfaces were specified as R_T^{exh} =

Table 1
Material properties of various components in the TEG system.

Components	Materials	Properties
Electrodes	Copper	$\lambda_{co} = 400$
Ceramic substrate	Alumina ceramic (96 %)	$\rho_{co} = 1.667 \times 10^{-8}$ $\lambda_{ce} = 27$
p-type leg	Bi_2Te_3 - based	$\lambda_p(T) = -5.8064 + 0.06157T$ $-1.6822 \times 10^{-4}T^2 + 1.5026 \times 10^{-7}T^3$ $\rho_p(T) = -7.1424 \times 10^{-6} + 4.2700 \times 10^{-8}T$ $\alpha_p(T) = 5.1772 \times 10^{-4} - 3.50126 \times 10^{-6}T$ $+ 1.0980 \times 10^{-8}T^2 - 1.06646 \times 10^{-11}T^3$
n-type leg	Bi_2Te_3 - based	$\lambda_n(T) = -5.9426 + 0.0637T$ $-1.7582 \times 10^{-4}T^2 + 1.6139 \times 10^{-7}T^3$ $\rho_n(T) = -2.8186 \times 10^{-6} + 3.0400 \times 10^{-8}T$ $\alpha_n(T) = -8.8933 \times 10^{-5} + 2.8700 \times 10^{-8}T$ $-1.6700 \times 10^{-9}T^2 + 2.5160 \times 10^{-12}T^3$

Table 2
Geometric parameters of different components.

Component	Geometry (L × W × H) mm
heat source	40 × 40 × 0.1
heat sink	40 × 40 × 0.1
ceramic substrate	40 × 40 × 0.7
copper electrode	3.8 × 1.4 × 0.4
p-type leg	1.4 × 1.4 × 1.6
n-type leg	1.4 × 1.4 × 1.6

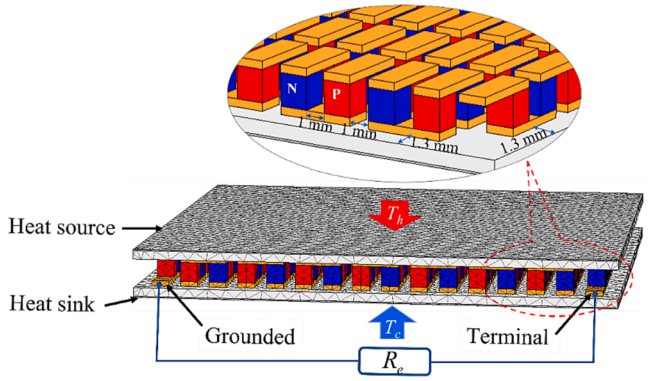

Fig. 2. The TEG components in the computational domain and the relevant boundary conditions.

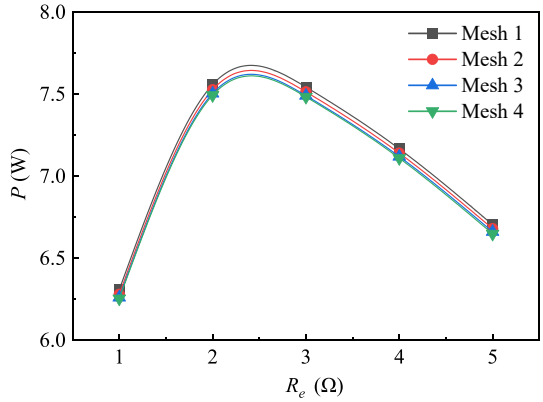

Fig. 3. The TEG output power obtained using different meshes.

2.01266×10^{-4} K·m^2/W, $R_T^{exc} = 1.47389 \times 10^{-4}$ K·m^2/W, $R_T^{inh} = 3.27624 \times 10^{-5}$ K·m^2/W, and $R_T^{inc} = 3.27624 \times 10^{-5}$ K·m^2/W. For the ECRs, they were set to $R_E = 8.32239 \times 10^{-10}$ Ω·m^2 on both the hot and cold sides. All these data are directly from the experiments [41].

As to the boundary conditions, the constant temperatures, T_h and T_c, were specified on the top surface of the heat source and the bottom surface of the heat sink, respectively. For the electric field, one copper electrode connecting to R_e was set at the ground state, whose electric potential $U = 0$ V.

It is also worth mentioning that after each simulation the TEG performance was assessed in terms of the output voltage, V, output power, P, and efficiency, η. For V, it was directly evaluated as the voltage on R_e. With it, P was computed by

$$P = \frac{V^2}{R_e}, \tag{12}$$

and the efficiency of TEG is defined by

$$\eta = \frac{P}{q \cdot A_h} \times 100\%. \tag{13}$$

q is the magnitude of the heat flux from the heat source to the TEG module. It was calculated based on the temperature gradient of the heat source.

3. Model verification

To guarantee the accuracy of the multi-physical model, mesh independence analysis and experimental validation are conducted in this section. To be specific, the mesh independence analysis is first carried out to make a trade-off between the numerical accuracy and computational efficiency of the simulations. Once the proper meshes are determined, the model is further validated by the available experimental results.

3.1. Mesh independence analysis

In the mesh independence tests, the predefined physics-controlled mesh method in COMSOL was used to allocate free tetrahedral meshes in the computational domain. In particular, four meshes with the mesh numbers $N = 13347$, 20211, 88165, and 141,149 were employed, which are referred to as Mesh 1, Mesh 2, Mesh 3 and Mesh 4 for convenience hereafter. Furthermore, the TEG output power was chosen as an indicator—we checked its convergence with the increasing mesh number. In simulation, the top-surface temperature of the heat source and the bottom-surface temperature of the heat sink were set as $T_h = 523$ K and $T_c = 305$ K, and the external load resistances R_e varied from 1 Ω to 5 Ω.

Fig. 3 compares the output power obtained using different meshes. It is clear that the difference of the numerical results at different meshes became smaller with the increasing mesh number. For example, we compared the output power at the five given external load resistances using Mesh 3 and Mesh 1. The relative errors (defined by $\left(\left|P_i^3 - P_i^1\right|\right)/P_i^3 \times 100\%$, where the superscripts 1 and 3 represent Mesh 1 and Mesh 3, while the subscript i denotes the i^{th} external load resistance among the five choices) in all cases were no more than 0.8%. When the results using Mesh 3 and Mesh 4 were compared, the corresponding relative errors further dropped below 0.2%. As a consequence, Mesh 3 has been adopted in the following numerical simulations as further finer meshes did not bring significant improvement.

3.2. Experimental validation

In this section, the numerical simulations were also validated by the experimental data which were obtained from a real TEG rig in our

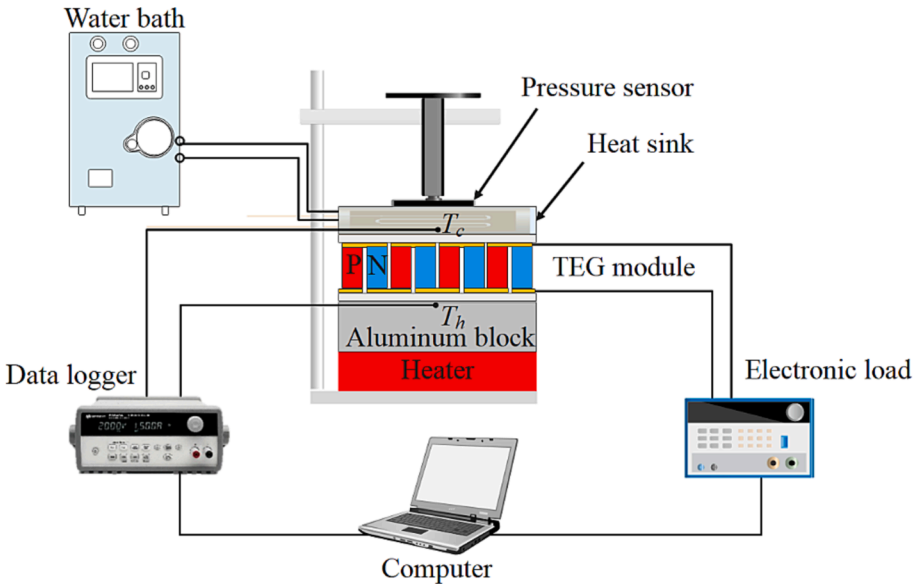

Fig. 4. The schematic diagram of the TEG test rig used in Ref. [41].

previous study [41]. As schematically shown in Fig. 4, it consists of a heater, a thermostatic water bath, a heat sink, a pressure controller with a pressure sensor, a TEG module, an electronic load, and a data logger. For direct comparison with experimental data, the five pairs of T_h and T_c used in the experiments have been set as the thermal boundary conditions in the simulations. Their detailed information is presented in Table 3. Moreover, the external resistance R_e used in these validations ranged from 0.5 Ω to 5 Ω.

Fig. 5 compares the output voltage and output power obtained by the numerical simulations in this work with the experimental data under the same TEG operating conditions [41]. It is seen that they are in good agreement in all the cases – the errors of the output power between the simulations and experiments were less than 3.0%, while they were further limited to 1.7% for the output voltage. These comparisons clearly demonstrate that the multi-physical model in Section 2 can numerically predict the TEG performance with good accuracy.

4. Results and discussion

In this section, we apply the validated model to 1) identify the TCR location (interface) which is the most influential to the TEG output power and efficiency; 2) reveal the difference in TEG performance obtained using distributed TCR and lumped TCR; 3) investigate the impacts of distributed TCR and ECR on TEG performance; 4) clarify the dependence of optimal heights of TE legs and copper electrodes on distributed TCR and ECR.

4.1. Impacts of the TCR locations on TEG performance

As discussed in Section 1, TCRs exist at different locations in a TEG, and each TCR location may pose different impacts on its performance. Therefore, our interest, first and foremost, is to identify the TCR location which exerts the most significant influence on TEG performance. To this end, we introduced a thermal resistance of $R_{T,0} = 0.31489$ K/W in the simulations. It is the overall thermal resistance from all interfaces of the TEG system obtained in our previous experiments [41]. This variable was then assigned to different locations in turn, including the external and internal hot-side and cold-side interfaces as shown in Fig. 1. In each case, the TCR at one specific location was specified by multiplying $R_{T,0}$ by the corresponding contact area (i.e., interfacial area). Meanwhile, the ECR of the TEG system was set to $R_{E,0} = 8.32239 \times 10^{-10}$ Ω·m^2, which was also from our experiments [41]. With all these settings, we performed numerical simulations using the proposed model in Section 2 and compared the resulting TEG output power and efficiency. Note that the comparisons in this section are based on the overall thermal resistance from all interfaces (i.e., $R_{T,0}$), rather than any given TCR. This is because TCR depends not only on thermal resistance but also on contact area, while the latter is different at different locations. Therefore, setting one overall TCR for different cases means that each of them has a distinct overall thermal resistance, making their comparisons meaningless. In this section, for convenience, the output power and efficiency are denoted by P_{exc} and η_{exc} when $R_{T,0}$ is located at the external cold-side interface. As to the cases with $R_{T,0}$ located at the external hot-side, internal hot- and cold-side interfaces, their output power and efficiency are represented by P_{exh} and η_{exh}, P_{inh} and η_{inh}, P_{inc} and η_{inc}, respectively.

Fig. 6 shows the obtained numerical results in these four cases at different top-surface temperatures of the heat source, T_h, and external load resistances, R_e. It is seen from Fig. 6(a) that P_{exc} is smaller than P_{exh} throughout the entire ranges of T_h and R_e; meanwhile, each of them is very close to their internal counterparts on the same side (i.e., P_{inc} and P_{inh}, respectively). The maximum output power under different T_h is further plotted in Fig. 6(b). It is shown that at a low T_h, e.g., $T_h = 342$ K, the maxima of P_{exc}, P_{inc}, P_{exh} and P_{inh} have almost the same values. However, these maximum values differed from one another with the increase of T_h, and the largest discrepancy of 9.5% occurred between P_{inh} and P_{exc} at $T_h = 523$ K.

As for the TEG efficiency, the best efficiency at each pair of T_h and R_e was obtained when the thermal resistance $R_{T,0}$ was located at the external hot-side interface. On the other hand, the TEG with $R_{T,0}$ at the external cold-side interface always suffered from the lowest efficiency, see Fig. 6(c). Furthermore, when the thermal resistance $R_{T,0}$ was on the cold side, regardless of the external or internal interface, the corresponding TEG efficiency was always smaller than its counterpart with $R_{T,0}$ on the hot side. Fig. 6(d) further illustrates the variations of the

Table 3
The operating conditions for validation tests.

Operating conditions	T_h(K)	T_c(K)
1	342	296
2	387	298
3	432	300
4	477	303
5	523	305

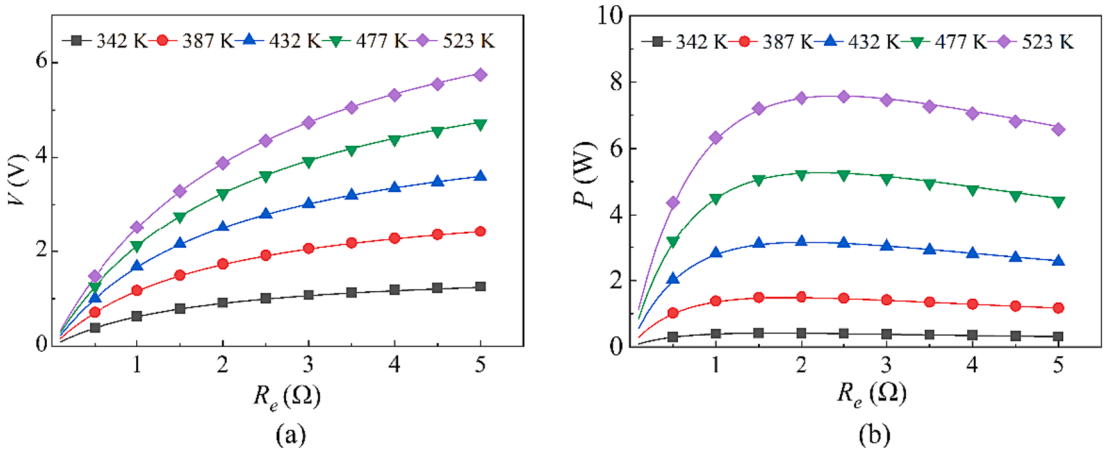

Fig. 5. Comparison of (a) the output voltage and (b) the output power between numerical and experimental results [41] under different R_e and T_h. Solid lines: numerical results; Symbols: experimental results.

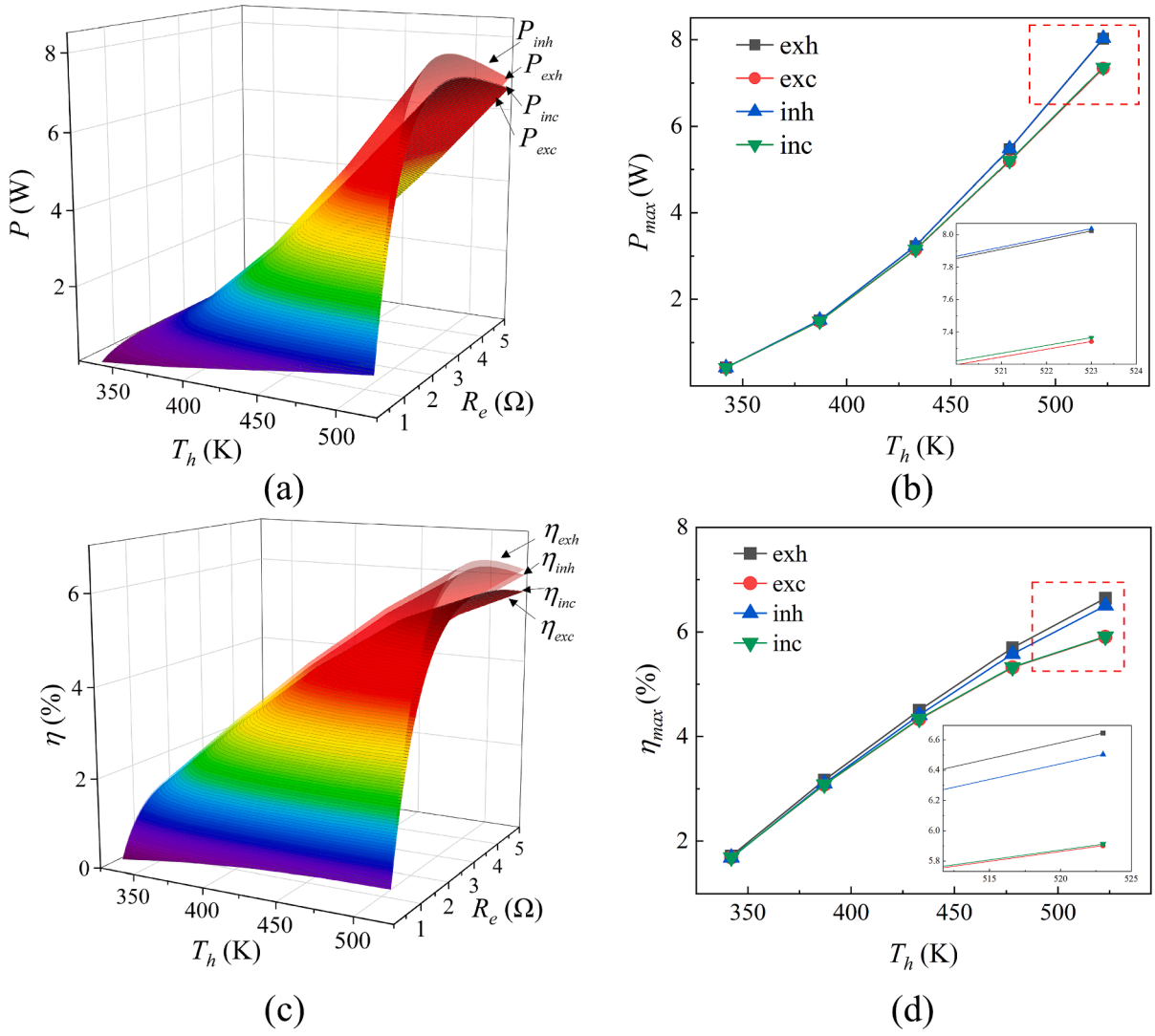

Fig. 6. Comparison of the TEG performance at different T_h and R_e with $R_{T,0}$ located at the four interfaces. (a) output power; (b) maximum output power; (c) efficiency; and (d) maximum efficiency.

maximum efficiency over a range of 342 K⩽T_h⩽523 K. It is found among the four cases that the largest discrepancy occurred between η_{exh} and η_{exc} at T_h = 523 K, which was 10.2%. Apparently, based on the results in Fig. 6(a)–6(d), the interfaces on the cold side exerted more significant impacts on the TEG output power and efficiency. Therefore, to improve TEG performance, we should more focus on minimizing the TCRs on this

particular side.

4.2. Comparison of TEG performance with distributed TCR and lumped TCR

The simulations in Section 4.1 revealed the importance of its location when we included the thermal resistance from the interfaces in the evaluation of TEG performance. However, such an overall thermal resistance was just assigned to one specific location at a time. This means that the corresponding TCR of the TEG system has been effectively reduced to a single lumped variable; its inherent distribution across different interfaces has been completely smeared out. In this section, we evaluate TEG performance based on this lumped-variable simplification, while comparing the results with those using the TCR distribution at different interfaces explicitly specified in Section 2.2. The difference in the TEG output power and efficiency of these two different TCR settings will be highlighted. For convenience, we will call them distributed and lumped TCR hereafter.

In the simulations using distributed TCR, as detailed by Section 2.2, four local TCRs, R_T^{exh}, R_T^{inh}, R_T^{exc} and R_T^{inc}, were specified at the external and internal hot- and cold-side interfaces, based on our previous experimental scenarios [41]. As to the simulations using lumped TCR, we repeated the procedure as described in Section 4.1, and obtained four cases with lumped TCRs at the external and internal hot- and cold-side interfaces, respectively. Note that all simulations corresponded to the same overall thermal resistance from all interfaces, i.e., $R_{T,0} = 0.31489$ K/W, and had the same ECR, i.e., $R_{E,0} = 8.32239 \times 10^{-10}$ Ω·m^2.

Fig. 7 shows the resulting TEG performance by our numerical simulations. To distinguish these results, the output power and efficiency obtained using distributed TCR have been denoted by P_{dis} and η_{dis}. In this section, P_{exc} and η_{exc}, P_{exh} and η_{exh}, P_{inh} and η_{inh}, P_{inc} and η_{inc} represent the output power and efficiency with the lumped TCRs located at the external cold-side, external hot-side, internal hot-side, and internal cold-side interfaces, respectively. For the TEG output power, appreciable differences of P_{dis} from P_{exh},P_{inh}, P_{exc} and P_{inc} are clearly observed in Fig. 7(a). To be specific, the average discrepancies between P_{dis} and its counterparts obtained with the lumped TCRs were 3.4%(P_{exh}),3.6%(P_{inh}), 1.8%(P_{exc}) and 1.8%(P_{inc}), respectively. In particular, the treatments of lumped TCR on the hot side, either at the external or internal interface, always resulted in larger TEG output power compared to the results with distributed TCR. Their maximum discrepancy could even jump to 16.9% at $T_h = 523$ K and $R_e = 0.1$ Ω. As to the TEG efficiency, similar phenomena are shown in Fig. 7(b). The average discrepancies between η_{dis} and η_{inc} was 0.9%, while for η_{exc},η_{inh} and η_{exh} such discrepancies have grown up to 4.2%, 8.7% and 11.0%, respectively. It was also found that larger efficiency was obtained in the simulations with lumped TCR on the hot side. Among all the results the largest discrepancy occurred between η_{exh} and η_{dis} with a value of 24.5% at $T_h = 523$ K and $R_e = 0.1$ Ω.

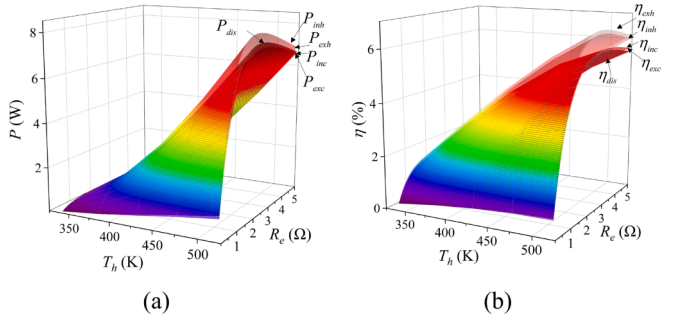

Fig. 7. Comparison of the TEG performance at different T_h and R_e with distributed TCR to that with lumped TCRs at different locations. (a) output power; (b) efficiency.

Based on the numerical results in this section, it is clearly demonstrated that the performance of TEG is indeed subject to its TCR distribution – even simplifying to a lumped TCR at different locations has led to different TEG output power and efficiency, not to mention that these results are significantly different from those obtained using distributed TCR. Therefore, it is no doubt that a reliable TEG performance evaluation requires effective characterization of TCR distributions. The model with distributed TCR proposed in this work well fits this need. Next, we will apply it to reveal more specific impacts of TCR and ECR on TEG performance and its structure.

4.3. Impacts of distributed TCR and ECR on TEG performance

In this section and Section 4.4, we conduct numerical simulations using the model with distributed TCR in Section 2. For brevity, unless stated otherwise, we simply refer to "distributed TCR" as "TCR" below. To investigate both the individual and joint impacts of TCR and ECR on the TEG output power and efficiency, four simulation cases were discussed in this section – Case "both" whose simulations considered both TCR and ECR; Case "TCR" and Case "ECR" were for the simulations including only TCR or ECR, respectively; for simulations with TCR and ECR ignored, they were simply denoted by Case "none". Fig. 8 shows the numerical results of these cases at different T_h and R_e.

To be specific, Fig. 8(a) compares the TEG output power, P, at different values of T_h and R_e in the four cases. For demonstration while without loss of generality, the detailed variations of P with different values of R_e at $T_h = 523$ K are further presented in Fig. 8(b). In general, the TEG output power, P, improved with the rise of T_h, but had the first-rising-and-then-falling variations with increasing R_e in the four cases. Meanwhile, at a given T_h and R_e, the value of P in Case "none" was always larger than its counterparts in the other three cases. The overestimation of the output power was at least 51.4% when Case "none" was compared with Case "both". This overestimation could further grow up to 112.3% at $T_h = 342$ K and $R_e = 0.1$Ω. Furthermore, when only ECR was taken into account, P was reduced by at least 5.6% as compared to that in Case "none"; such a reduction elevated to the maximum at 23.6% when T_h and R_e dropped to 342 K and 0.1 Ω. As to TCR, it has a more significant negative influence on the output power than ECR. In comparison with Case "none", the minimal reduction of P in Case "TCR" was 29.7% at $T_h = 342$ K and $R_e = 5$ Ω, while the maximum was 39.8% at $T_h = 342$ K and $R_e = 0.1$ Ω. It is evident that the output power suffered from a more substantial decline by TCR than ECR.

The impacts of TCR and ECR on the TEG efficiency, η, is also studied. Fig. 8(c) shows the changes of η in the four simulation cases at different values of T_h and R_e. It can be seen that the neglect of TCR or ECR also caused an overestimation in the TEG efficiency at all the given values of T_h and R_e. In Case "none", the values of η were exaggerated by 31.0% (at $T_h = 523$ K and $R_e = 5$ Ω) to 69.3% (at $T_h = 342$ K and $R_e = 0.1$ Ω) in comparison with those in Case "both", and 4.9%(at $T_h = 523$ K and $R_e = 5$ Ω) to 19.3% (at $T_h = 342$ K and $R_e = 0.1$ Ω) in comparison with those in Case "ECR". In Case "TCR", its efficiency was at least 19.8% lower than that in Case "none", and at $T_h = 342$ K and $R_e = 0.1$ Ω such efficiency deterioration has surged as large as 27.1%. Apparently, TCR is a more unfavourable contributing factor to the TEG efficiency.

It is worth noting that at a given T_h the output power and efficiency can reach their maxima if the external load resistance, R_e, is properly adjusted (This is the so-called matching of external load resistance in the TEG studies). To be specific, when the external load resistance is the same as the internal electric resistance of the TEG module, i.e., $R_e^o = R_{TEG}$, the TEG will deliver the maximum output power, $P_{\max}$. If the external load resistance, R_e^{oo}, is equal to $\sqrt{1+Z_{eff}\overline{T}}R_{TEG}$, the TEG will achieve the maximum efficiency, $\eta_{\max}$ [48]. Here the two external load resistances, corresponding to $P_{\max}$ and $\eta_{\max}$, have been specifically denoted as R_e^o and R_e^{oo}, respectively. Since precise matching of external load resistance is crucial to achieve $P_{\max}$ and $\eta_{\max}$ of a TEG, it is

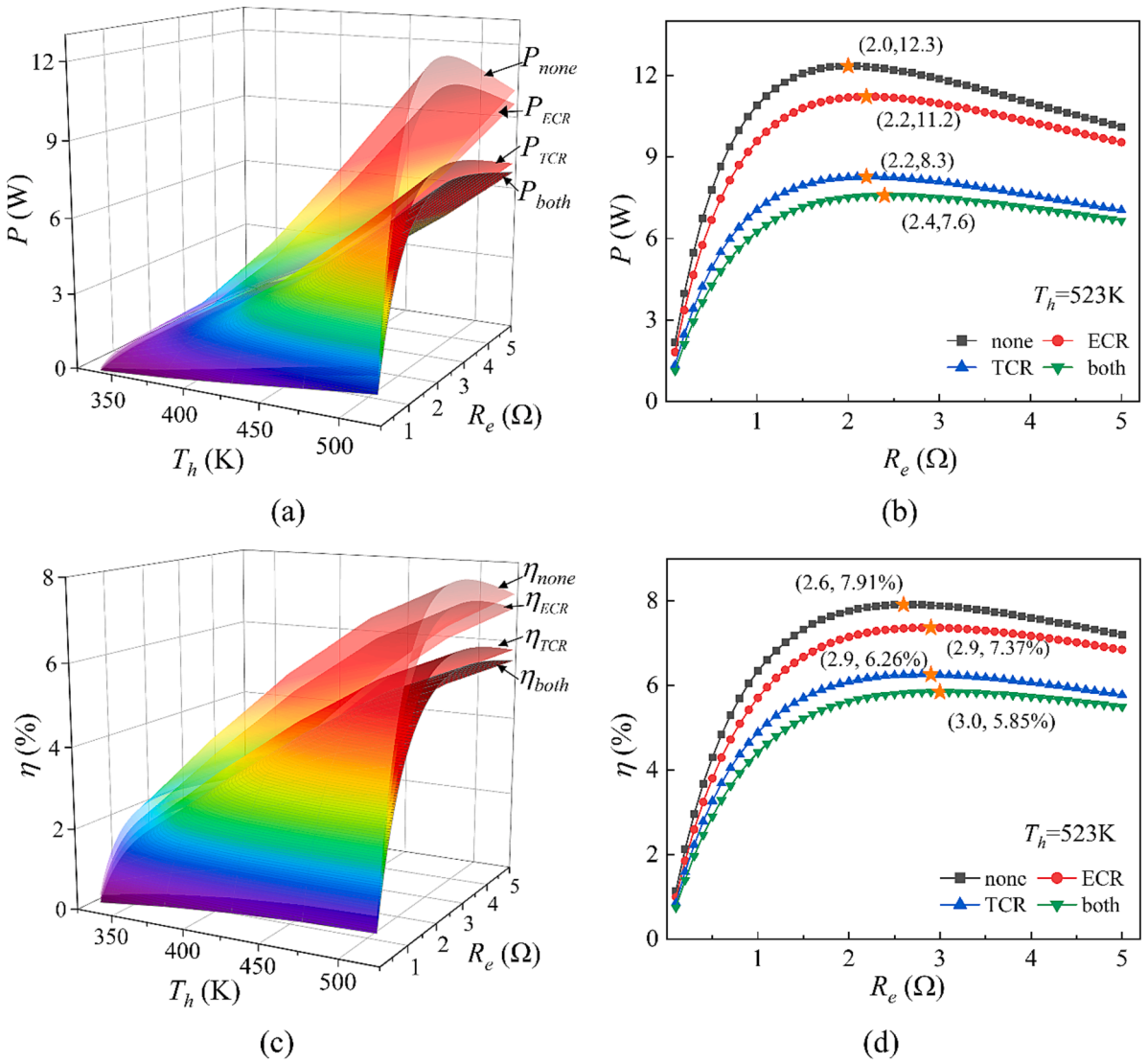

Fig. 8. The variations of the TEG output power ((a) and (b)) and efficiency ((c) and (d)) in different cases. The pair of numbers in parentheses near each orange star denotes the external load resistance and the maximum output power (Fig. 8(b)) or the maximum efficiency (Fig. 8(d)) achieved at that load. (For interpretation of the references to colour in this figure legend, the reader is referred to the web version of this article.)

significant to investigate whether such a process is affected by TCR and/or ECR. To this end, the TEG output power and efficiency of the four simulation cases were evaluated by simulation at different external load resistances but at a constant top-surface temperature of the heat source. For simplicity without losing generality, we only displayed the results at T_h = 523 K in Fig. 8(b) and 8(d), and marked R_e^o and R_e^{oo} in the four cases. As shown in Fig. 8(b), the magnitudes of R_e^o in Case "ECR", Case "TCR" and Case "both" were 10%, 10% and 20% larger than that in Case "none". In Fig. 8(d), such increases of R_e^{oo} in the former three cases were 12%, 12%, and 15% in comparison with that in Case "none". These results can be well explained – the inclusion of ECR directed to a larger R_{ipara}. As to TCR, it affected the temperature distributions in the TE materials, thereby changing their temperature-dependent electric properties (N.B.: more details will be illustrated in Fig. 9). All these changes eventually led to the growth of R_{TEG}, too.

Next, we study how the maximum output power, P_{max}, and maximum efficiency, η_{max}, vary with different values of TCR and ECR. To this end, the external load resistance in the simulation was properly matched to achieve P_{max} and η_{max}, when TCR (or ECR) was tuned to 100%, 80%, 60%, 40%, and 20% of its original magnitude, while ECR (or TCR) was kept unchanged. In each case, P_{max} were computed at different values of T_h, and are shown in Fig. 9(a) and 9(c). It is seen that P_{max} improved when either TCR or ECR decreased. For instance, when TCR was only 20% of its original magnitude, P_{max} increased averagely by 35.6% at all T_h. As for ECR, the reduction to 20% of its original magnitude led to an average improvement of 8.8% in P_{max} over the range of T_h = 342 K to T_h = 523 K. We point out that although the reductions of TCR and ECR both brought the improved P_{max}, their underlying mechanisms are completely different. Here for illustration, we take the results at T_h = 523 K as an example; Similar findings are also obtained at T_h = 342, 378, 432 and 477 K. Fig. 9(b) and 9(d) show the temperature details of the TE legs with different values of TCR and ECR, respectively. It is shown that with the decrease of TCR, the hot-side temperature of TE legs, T_{hl} , gradually increased, while its counterpart on the leg cold side, T_{cl}, decreased. This signifies that the temperature difference between these two sides, ΔT_l, did increase as TCR decreased. Based on Eq. (1) it is not surprising that P_{max} grew in these cases accordingly. As to ECR, its reduction had little effect on T_{hl} and T_{cl}, thereby their differences, ΔT_l, were almost unchanged as shown in Fig. 9(d). Under this circumstance, the growth in P_{max} mainly caused by the reduction of the TEG electric resistance, R_{TEG}, due to the decreasing ECR.

Also, variations of the maximum efficiency, η_{max}, with different

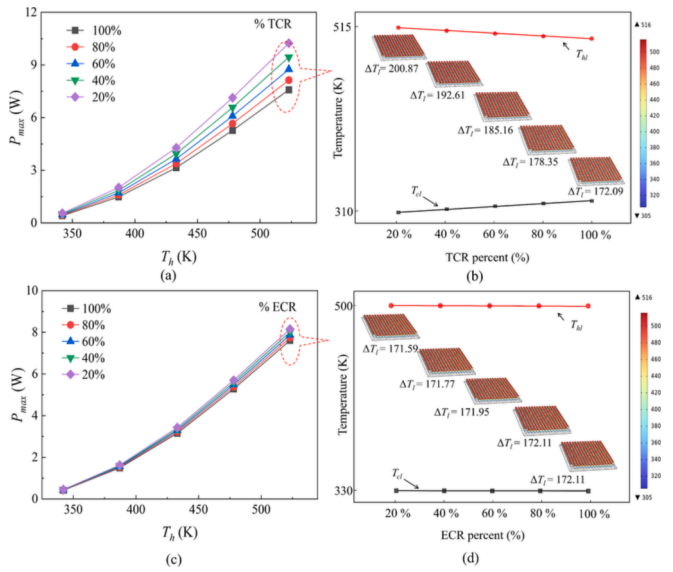

Fig. 9. The variations of P_{max} and ΔT_l with different values of TCR and ECR. (a) P_{max} at different T_h with different values of TCR; (b) temperature differences across TE legs with different values of TCR ($T_h = 523$ K); (c) P_{max} at different T_h with different values of ECR; (d) temperature differences across TE legs with different values of ECR ($T_h = 523$ K).

values of TCR and ECR are investigated. See Fig. 10, where similar effects were observed on $\eta_{\max}$ as TCR or ECR decreased. As shown in Fig. 10(a) and 10(c), smaller TCR or ECR always led to larger $\eta_{\max}$. To be specific, when the values of TCR or ECR were reduced to 20% of its original magnitudes, $\eta_{\max}$ improved by 16.8% and 6.9% on average, respectively. Note that $\eta_{\max}$ depends on $Z_{eff}\overline{T}$, T_{hl}, and T_{cl}, as shown in Eq. (2), while such dependences are non-linear and non-monotonic. To facilitate a straightforward explanation, we still take $T_h = 523$ K as an example, and display its heat input and output power (as shown by Eq. (13)) with different values of TCR and ECR in Fig. 10(b) and 10(d). Under this thermal condition, both the heat input and output power gradually increased with the decreasing TCR, as shown in Fig. 10(b). In particular, the increase of the latter was much more significant. Finally, their competing effects resulted in a growing maximum efficiency with the decreasing TCR. As to ECR, the output power presented a nearly linear growth with its reduction. This is totally different from the corresponding heat input, which remained almost unchanged regardless of the value of ECR. It is shown that although $\eta_{\max}$ did grow with the decreasing ECR, its growth was much smaller in comparison with its counterpart by the TCR reduction.

So far, our numerical simulations elaborate the negative impacts of TCR and ECR on the TEG performance at different values of T_h and R_e. They show that the TEG performance degradation is more sensitive to TCR than ECR. Moreover, these simulations reveal that the inclusion of TCR and/or ECR can impact the matching of external load resistances and lead to different values of R_e^o and R_e^{oo}, which correspond to $P_{\max}$ and $\eta_{\max}$, respectively.

4.4. Impacts of distributed TCR and ECR on TEG geometric optimization

Besides the direct impacts on the TEG performance elaborated in the previous sections, TCR and ECR also play an important role in designing and optimizing TE legs and copper electrodes. Note that a TEG with or without TCR and ECR may have different optimal sizes for its TE legs and copper electrodes when the maximum output power or maximum efficiency is used as its optimization objective. Therefore, in this section, a series of geometric optimizations of TE legs and copper electrodes are performed with TCR and ECR. Comparison to those without considering TCR and ECR is also presented.

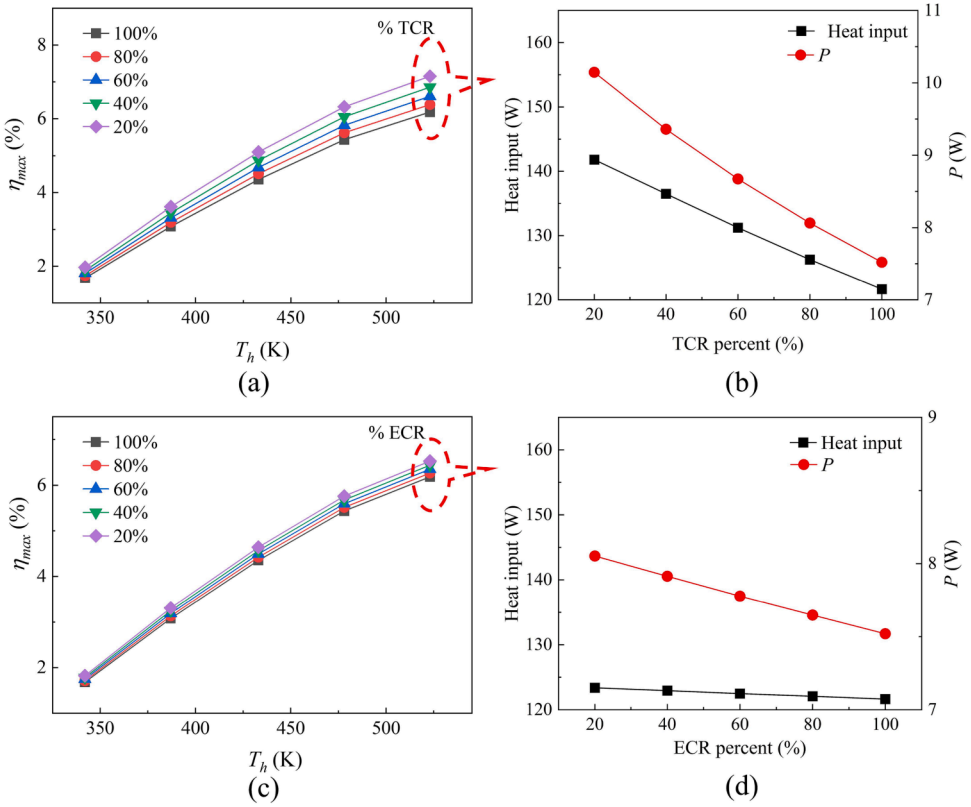

Fig. 10. The variations of η_{max}, P and heat input with different values of TCR and ECR and at different T_h . (a) η_{max} with different values of TCR; (b) heat input and P with different values of TCR ($T_h = 523$ K); (c) η_{max} with different values of ECR; (d) heat input and P with different values of ECR ($T_h = 523$ K).

4.4.1. Thermoelectric leg height

We first evaluated the TEG maximum output power, P_{max}, at different leg heights, h_l, and different T_h. The results with and without TCR and ECR are shown in Fig. 11(a) and 11(b). Note that the lengths and widths of TE legs were unchanged in our simulations, and the other geometrical components were set as shown in Table 2. Fig. 11(a) shows a non-monotonic dependence of P_{max} on h_l with TCR and ECR considered. To be specific, P_{max} first had a sharp growth with the increasing h_l, and then declined gradually with its further increase. In this case, we can clearly observe the peak value of P_{max}, and identify the corresponding optimal leg height, h_l^0—it was 0.6 mm and independent of T_h. In contrast, the results without TCR and ECR are exhibited in Fig. 11(b), where P_{max} just declined with the increase of h_l at any T_h. Apparently, there was no optimal leg height, and the leg height need to be as short as possible to avoid a dramatic decline of P_{max}. As to the scenarios using the maximum efficiency, η_{max}, as the optimization objective, Fig. 11(c) and 11(d) show its variations at different values of h_l and T_h with and without TCR and ECR. In general, a larger leg height led to better maximum efficiency at all given T_h, regardless of whether TCR and ECR have been taken into account or not. Nevertheless, a closer look at Fig. 11(c) shows that when TCR and ECR were included, η_{max} gradually and slowly increased with the increasing h_l. As to the cases neglecting TCR and ECR, their η_{max} first had sharper growth with h_l when $h_l < 0.5$ mm. Its growth rate then slowed down with the further increase of h_l.

Moreover, Fig. 11 also shows that at a given h_l and T_h, the values of P_{max} and η_{max} were largely overestimated when TCR and ECR were neglected. Take a comparison of the two cases with and without TCR and ECR at $h_l = 0.6$ mm and $T_h = 523$ K—the values of P_{max} and η_{max} in the latter have been overrated by 193.8% and 78.3% in comparison to their counterparts in the former. In fact, the overestimations of P_{max} and η_{max} were at least 31.9% and 15.3% over the ranges of 0.1 mm$\leqslant h_l \leqslant$3 mm and 342 K$\leqslant T_h \leqslant$523 K. They even became more significant at a shorter h_l or/and a lower T_h. In addition, the optimal leg height, h_l^o, specified in Fig. 11(a), does not correspond to the peak value of η_{max}. This means that there does not exist a single leg height that can achieve the peak values of both P_{max} and η_{max}. Therefore, a trade-off is desired in the practical optimization of TE leg height so that the TEG can have reasonably balanced maximum output power and maximum efficiency. In short, from all the aforementioned discussion based on Fig. 11, it is clear that TCR and ECR did play a non-negligible role. Simply ignoring them could mislead the design and optimization of TE legs.

4.4.2. Copper electrode height

In a TEG, the copper electrode height, h_c, is another factor affecting its performance, as this geometric property impacts not only the temperature difference upon TE legs but also the TEG electric resistance. Therefore, it is worth investigating how TEG performance (in terms of P_{max} and η_{max}) behaves with different h_c when TCR and ECR are presented. To this end, we conducted a series of simulations with those given values of TCR and ECR and evaluate the values of P_{max} and η_{max} at 0.05 mm$\leqslant h_c \leqslant$2 mm and 342 K$\leqslant T_h \leqslant$523 K. These results are then compared with those when TCR and ECR have been ignored.

We first conducted the numerical simulations at the condition that TE legs were at their optimal heights, i.e., $h_l = h_l^o = 0.6$ mm. Fig. 12(a)

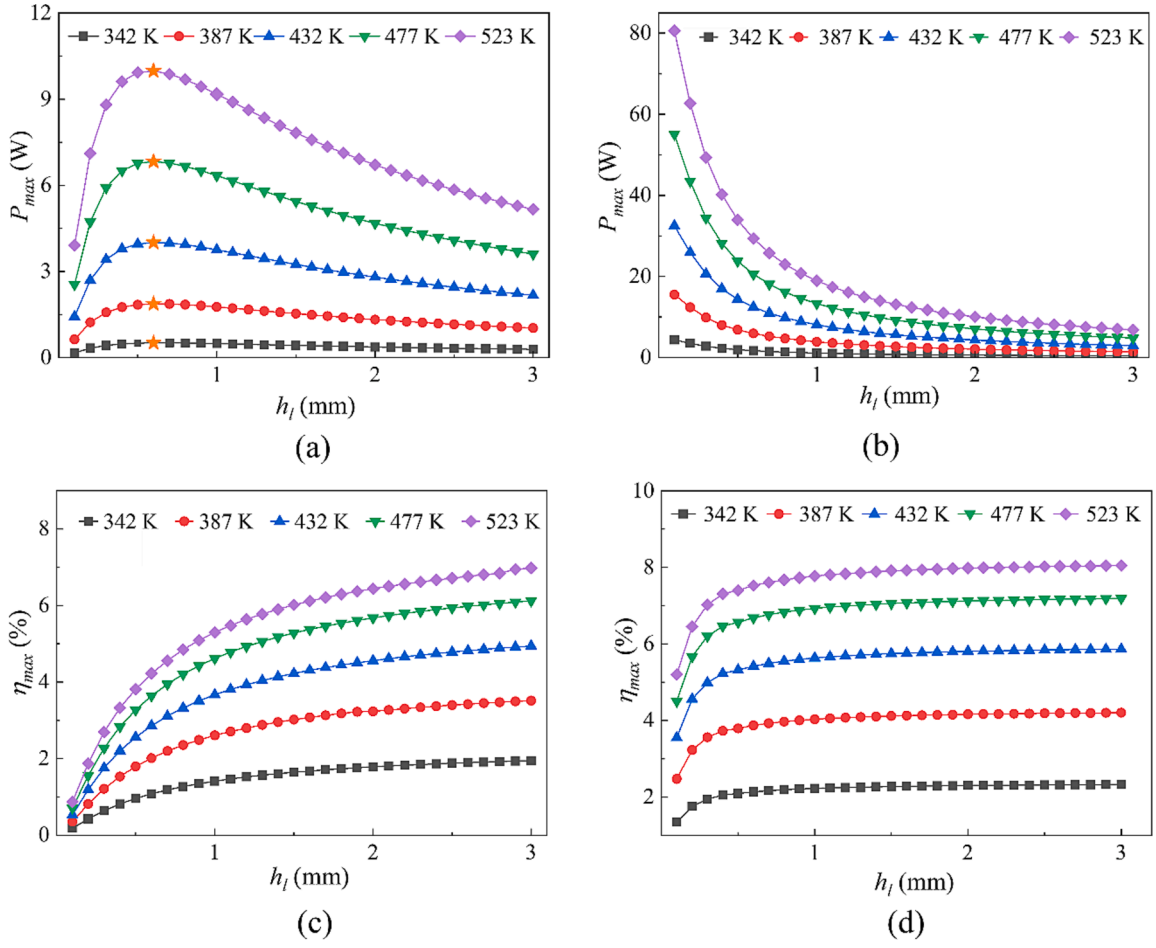

Fig. 11. The variations of P_{max} and η_{max} at different h_l and T_h. (a) P_{max} with TCR and ECR; (b) P_{max} without TCR and ECR; (c) η_{max} with TCR and ECR; (d) η_{max} without TCR and ECR. The orange stars highlight the peak values of P_{max}. (For interpretation of the references to colour in this figure legend, the reader is referred to the web version of this article.)

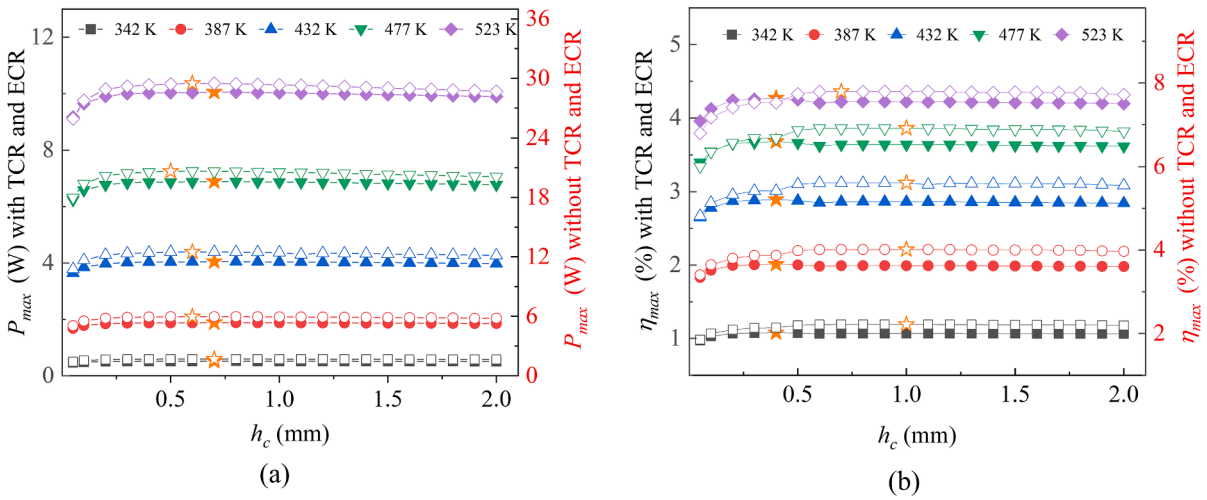

Fig. 12. The variations of P_{max} and η_{max} with h_c at $h_l = 0.6$ mm and different T_h. (a). P_{max} with and without TCR and ECR; (b) η_{max} with and without TCR and ECR. With TCR and ECR: solid symbols; Without TCR and ECR: hollow symbols. Peak values: orange stars. (For interpretation of the references to colour in this figure legend, the reader is referred to the web version of this article.)

shows the resulting $P_{\max}$ with and without TCR and ECR at $h_l = 0.6$ mm. Under both conditions, regardless of the value of T_h, $P_{\max}$ first increased and then slightly decreased with the increase of h_c. Therefore, there existed an optimal copper electrode height, h_c^o, at which $P_{\max}$ reached its peak at a given T_h(see those orange stars marked in Fig. 12). It was found that when TCR and ECR were included, the value of h_c^o was always equal

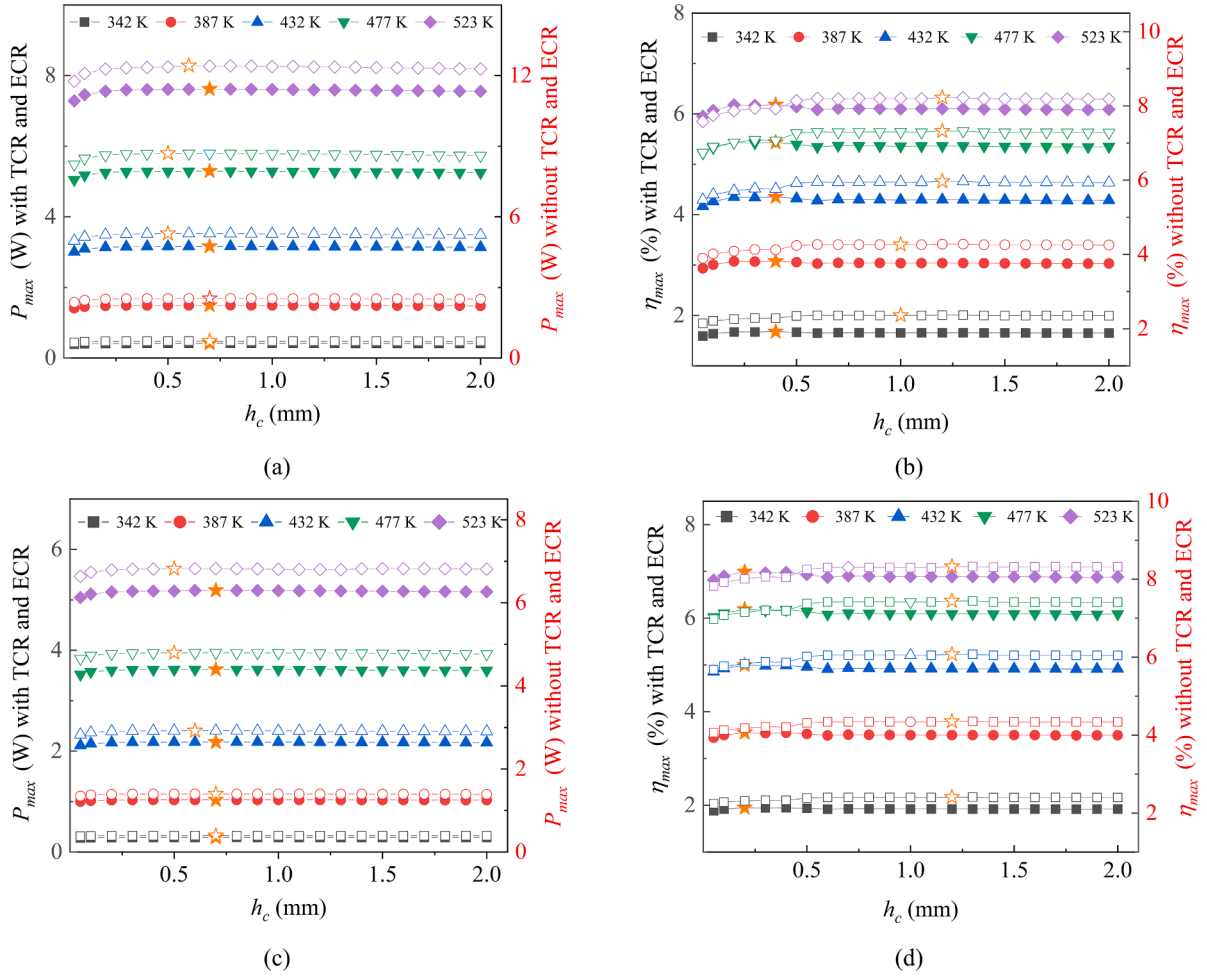

Fig. 13. The variations of P_{max} and η_{max} with h_c at different T_h. (a). P_{max} with and without TCR and ECR at $h_l = 1.6$ mm; (b) η_{max} with and without TCR and ECR at $h_l = 1.6$ mm; (c) P_{max} with and without TCR and ECR at $h_l = 3.0$ mm; (d) η_{max} with and without TCR and ECR at $h_l = 3.0$ mm. With TCR and ECR: solid symbols; Without TCR and ECR: hollow symbols. Peak values: orange stars. (For interpretation of the references to colour in this figure legend, the reader is referred to the web version of this article.)

to 0.7 mm at every T_h. However, it was no longer constant but fell into the range of 0.5 −0.7 mm when TCR and ECR were neglected. It is important to note that any TEG in practical use inherently has both TCR and ECR. Therefore, simply using the value of h_c^o derived from the simplification that ignores TCR and ECR may lead to its P_{max} different from its actual peak (obtained when TCR and ECR are considered). Fortunately, our simulations show such a deviation was less than 0.4%.

To be similar, the maximum efficiency, η_{max}, was also calculated in the same TEG operating conditions with and without TCR and ECR, see Fig. 12(b). Particular attention was paid to the optimal copper-electrode height, h_c^{oo}, corresponding to the peak of η_{max} at each T_h. It is found that this optimal copper-electrode height was a constant, i.e., $h_c^{oo} = 0.4$ mm, at all T_h when TCR and ECR were considered. However, in the cases without TCR and ECR as shown in Fig. 12(b), it varied from 0.7 to 1.0 mm at different T_h. Similarly, the value of h_c^{oo} derived from the simplification that ignores TCR and ECR was used to specify η_{max} of the real TEG in our experiment. It is found that the results were different by more than 1% in comparison with its actual efficiency peak (i.e., when both TCR and ECR were considered). These results indicate that the conditions with or without TCR and ECR have an essential impact.

In this section, to make the optimization of copper electrodes closer to the TEG practical scenarios, we further extended our numerical simulations to the cases with $h_l = 1.6$ mm and 3.0 mm. Both are the TE leg heights widely used in the current commercialized TEG module. Fig. 13 exhibits the resulting P_{max} and η_{max} with different h_c, together with those obtained when TCR and ECR have been ignored for comparison. As shown in Fig. 13 (a) and (c), regardless of whether TCR and ECR have been considered, P_{max} at the conditions of $h_l = 1.6$ mm and 3.0 mm first increased gradually and then slightly reduced as h_c increased. Interestingly, for the corresponding optimal copper-electrode height h_c^o (at which P_{max} reached its peak), its values using these long TE legs are the exactly same as that obtained at $h_l = 0.6$ mm − it ranged between 0.5 and 0.7 when all contact resistances were ignored, while it was equal to 0.7 mm with both TCR and ECR considered. In this section, we also specified P_{max} of the real TEG in our experiment (with TCR and ECR) using h_c^o derived from the simplification that ignores TCR and ECR. The resulting deviations from the actual peak of P_{max} (i.e., those marked by orange solid stars in Fig. 13(a) and (c)) are less than 0.2%(for $h_l = 1.6$ mm) and 0.12%(for $h_l = 3.0$ mm). Apparently, these results, together with those at $h_l = 0.6$ mm, indicate that if the maximum output power is the optimization objective for a TEG using long TE legs ($h_l \geqslant 0.6$ mm), its TCR and ECR are not essential contributing factors to the optimization of copper-electrode heights.

Now we turn our attention to copper-electrode optimization using maximum efficiency, η_{max}, as the optimization objective. The results in the conditions of $h_l = 1.6$ mm and 3.0 mm are shown in Fig. 13(b) and (d). In general, the variations of η_{max} with h_c are very similar to those with $h_l = 0.6$ mm, and the optimal copper-electrode height corresponding to the peak of η_{max}, h_c^{oo}, has been clearly identified. At each T_h, $h_c^{oo} = 0.4$ mm ($h_l = 1.6$ mm) and 0.2 mm ($h_l = 3.0$ mm) when both TCR and ECR were considered. When all the contact resistances were ignored, the values of h_c^{oo} fell into the range between 1.0 mm and 1.2 mm. Again, we applied the latter h_c^{oo} to specify η_{max} of the real TEG used in our experiment. It is shown that its values were different by more than 1.2% (at $h_l = 1.6$ mm) and 1.5% (at $h_l = 3.0$ mm) from the actual efficiency peak. These results, together with those obtained at $h_l = 0.6$ mm, indicate that the copper-electrode optimization at $h_l \geqslant 0.6$ mm was affected by TCR and ECR in the TEG, if the corresponding optimization objective was the maximum efficiency.

5. Conclusion

It is known that TCR and ECR have substantial impacts on TEG performance and its geometric optimization. However, many previous studies either neglected them or described such impacts based on simplifying TCR as a single lumped variable, neglecting its intrinsic distribution across different interfaces in a TEG. In this study, the effects of TCR and ECR have been numerically investigated by a multi-physical model which not only includes both contact resistances but also specifies the TCR distribution based on our experimental results. The numerical simulations pinpointed the TCR location that exerts the most significant impact on TEG performance, and revealed distinct TEG output power and efficiency obtained using distributed TCR and lumped TCR. Following these findings, we conducted more detailed analyses on the individual and joint effects of distributed TCR and ECR on TEG performance. Our numerical simulations were also extended to the geometric optimization of TE legs and copper electrodes for the maximization of output power and efficiency, respectively. The main outcomes of our numerical study are concluded as follows:

1) Treating TCR as a lumped variable is simple; however, where this simplified TCR is allocated does affect the TEG output power and efficiency. In particular, it is found the TEG performance based on this widely-used treatment is different from that using more realistic distributed TCRs across different interfaces. The largest discrepancies between these two cases reach up to 16.9% (TEG output power) and 24.5% (TEG efficiency) at $T_h = 523$ K and $R_e = 0.1$ Ω. These results indicate that not only the magnitudes of TCR but also its distributions do matter to TEG performance.
2) For a given amount of thermal resistance at the four TCR interfaces, it affects TEG performance more significantly when located on the cold side, rather than the hot side. Moreover, such thermal resistance at either the external or internal interface on one side (regardless of the hot or cold side) exerts nearly identical effects on TEG performance. Therefore, reducing thermal resistance at the cold-side interfaces is more effective to improve TEG performance.
3) Both TCR and ECR have negative impacts on the output power and efficiency of a TEG. Conventional treatment of neglecting these contact resistances may mislead the TEG performance assessment. The numerical simulations in this article revealed that neglecting TCR and ECR caused the TEG output power and efficiency to be overestimated by at least 51.4% and 31.0%, respectively, under the given working conditions. These overestimations even soared to 112.3% and 69.3% at $T_h = 342$ K and $R_e = 0.1\Omega$. Also, neglecting TCR and ECR could lead to smaller optimal external load resistances matched for maximum output power and maximum efficiency, as compared with the real TEG operation where TCR and ECR are unavoidable. It is plain that a high-accuracy assessment of TEG performance necessitates clear specifications of TCR and ECR at all interfaces.
4) In comparison to ECR, TCR exerted more significant impacts on TEG performance. It was found that when TCR reduced to 20% of its original magnitude, the TEG maximum output power and maximum efficiency could increase by 35.6% and 16.8% on average, respectively. If ECR reduced to 20% of its original magnitude, such increases in the TEG maximum output power and maximum efficiency were just 8.8% and 6.9% on average, respectively. These findings indicate that TCR and its reduction are of more importance for a TEG system to improve its performance.
5) TCR and ECR had significant impacts on the geometric optimization of TE legs. To be specific, the optimal heights of TE legs for maximum output power were quite distinct in the cases with or without TCR and ECR. To achieve the peak value of the maximum output power, the optimal height $h_l^o = 0.6$ mm in the former while this geometric property was suggested as short as possible in the latter. If the maximum efficiency was used to characterize the TEG performance, long TE legs became preferable. This is because the maximum efficiency increased with the increasing TE leg height, no matter whether TCR and ECR were considered or not. It is no doubt that the optimization of TE legs should consider the impacts of TCR and ECR,

in particular when the maximum output power is chosen as the optimization objective.

6) As to copper electrodes, TCR and ECR had limited impacts on their geometric optimization. Our simulations show that the optimal copper electrode heights corresponding to the maximum output power, h_c^o, were very close to each other in the cases with or without TCR and ECR; In TEG applications at $h_l \geqslant 0.6$ mm, simply using h_c^o derived from the simplification that ignores TCR and ECR only caused the discrepancies in P_{max} from its peak values by less than 0.4%. As to the optimal copper electrode heights corresponding to the maximum efficiency, h_c^{oo}, its magnitudes differed by a few hundred micrometers with and without TCR and ECR; In this scenario, using h_c^{oo} derived from the simplification that ignores TCR and ECR has led to the maximum efficiency that differed from its actual peak values by more than 1%. Based on these results, it is concluded that at $h_l \geqslant 0.6$ mm, TCR and ECR can be safely neglected in the optimization of copper electrodes for the TEG maximum output power; however, they should be included when the optimization objective is the maximum efficiency.

CRediT authorship contribution statement

Ying Li: Writing – original draft, Validation, Methodology, Investigation, Formal analysis, Data curation, Conceptualization. **Yong Shi:** Writing – review & editing, Supervision, Resources, Methodology, Investigation, Formal analysis, Conceptualization. **Ding Luo:** Writing – review & editing, Conceptualization. **Xuehui Wang:** Writing – review & editing, Methodology. **Yuying Yan:** Supervision, Project administration, Funding acquisition.

Declaration of competing interest

The authors declare that they have no known competing financial interests or personal relationships that could have appeared to influence the work reported in this paper.

Data availability

Data will be made available on request.

Acknowledgments

The authors are grateful for the financial support from the Ningbo Science and Technology Bureau's Technology under Grant No. 2019B10042. Ying Li acknowledges the financial support from China Scholarship Council (CSC).

References

[1] R.A. Kishore, A. Nozariasbmarz, B. Poudel, S. Priya, High-performance thermoelectric generators for field deployments, ACS Appl. Mater. Interfaces 12 (2020) 10389–10401.
[2] M.H. Jeong, K.C. Kim, J.S. Kim, K.J. Choi, Operation of wearable thermoelectric generators using dual sources of heat and light, Adv. Sci. 9 (2022) e2104915.
[3] W. Ren, Y. Sun, D. Zhao, A. Aili, S. Zhang, C. Shi, J. Zhang, H. Geng, J. Zhang, L. Zhang, C. Xiao, R. Yang, High-performance wearable thermoelectric generator with self-healing, recycling, and Lego-like reconfiguring capabilities, Sci. Adv. 7 (2021) eabe0586.
[4] D. Kim, D. Ju, K. Cho, Heat-sink-free flexible organic thermoelectric generator vertically operating with chevron structure, Adv. Mater. Technol. 3 (2018) 1700335.
[5] S. Khanmohammadi, M.M. Baseri, P. Ahmadi, A.A.A.A. Al-Rashed, M. Afrand, Proposal of a novel integrated ocean thermal energy conversion system with flat plate solar collectors and thermoelectric generators: energy, exergy and environmental analyses, J. Clean. Prod. 256 (2020) 120600.
[6] M.Z. Malik, F. Musharavati, S. Khanmohammadi, M.M. Baseri, P. Ahmadi, D. D. Nguyen, Ocean thermal energy conversion (OTEC) system boosted with solar energy and TEG based on exergy and exergo-environment analysis and multi-objective optimization, Sol. Energy 208 (2020) 559–572.
[7] A. Riahi, A. Ben Haj Ali, A. Fadhel, A. Guizani, M. Balghouthi, Performance investigation of a concentrating photovoltaic thermal hybrid solar system combined with thermoelectric generators, Energy Convers. Manage. 205 (2020) 112377.
[8] S. Shittu, G. Li, Q. Xuan, X. Xiao, X. Zhao, X. Ma, Y.G. Akhlaghi, Transient and non-uniform heat flux effect on solar thermoelectric generator with phase change material, Appl. Therm. Eng. 173 (2020) 115206.
[9] D. Kraemer, B. Poudel, H.P. Feng, J.C. Caylor, B. Yu, X. Yan, Y. Ma, X. Wang, D. Wang, A. Muto, K. McEnaney, M. Chiesa, Z. Ren, G. Chen, High-performance flat-panel solar thermoelectric generators with high thermal concentration, Nat. Mater. 10 (2011) 532–538.
[10] B. Nie, W. Zhang, X. Dou, Y. Meng, X. Zhao, Y.-C. Wu, H.-J. Li, A porous dome array evaporator for high-performance photothermal water evaporation and thermoelectric power generation, J. Mater. Chem. A 12 (2024) 293–302.
[11] K. Huang, B. Li, Y. Yan, Y. Li, S. Twaha, J. Zhu, A comprehensive study on a novel concentric cylindrical thermoelectric power generation system, Appl. Therm. Eng. 117 (2017) 501–510.
[12] B. Li, K. Huang, Y. Yan, Y. Li, S. Twaha, J. Zhu, Heat transfer enhancement of a modularised thermoelectric power generator for passenger vehicles, Appl. Energy 205 (2017) 868–879.
[13] C.R.S. Rodrigues, T. Machado, A.L. Pires, B. Chaves, F.S. Carpinteiro, A.M. Pereira, Recovery of thermal energy released in the composting process and their conversion into electricity utilizing thermoelectric generators, Appl. Therm. Eng. 138 (2018) 319–324.
[14] J. Liu, S. Yadav, S.C. Kim, Performance of a thermoelectric generator system for waste heat recovery utilizing plate fin heat sink in bronze ingot casting industry, Case Stud. Therm. Eng. 38 (2022) 102340.
[15] G.N. Li, Y.Q. Zheng, J.E. Hu, W.W. Guo, Experiments and a simplified theoretical model for a water-cooled, stove-powered thermoelectric generator, Energy 185 (2019) 437–448.
[16] X.F. Zheng, C.X. Liu, R. Boukhanouf, Y.Y. Yan, W.Z. Li, Experimental study of a domestic thermoelectric cogeneration system, Appl. Therm. Eng. 62 (2014) 69–79.
[17] X.F. Zheng, Y.Y. Yan, K. Simpson, A potential candidate for the sustainable and reliable domestic energy generation–thermoelectric cogeneration system, Appl. Therm. Eng. 53 (2013) 305–311.
[18] M. Hodes, Optimal pellet geometries for thermoelectric power generation, IEEE Trans. Compon. Packag. Technol. 33 (2010) 307–318.
[19] X. Wang, H. Wang, W. Su, F. Mehmood, J. Zhai, T. Wang, T. Chen, C. Wang, Geometric structural design for lead tellurium thermoelectric power generation application, Renew. Energy 141 (2019) 88–95.
[20] J. Zhang, W. Zhang, H. Wei, J. Tang, D. Li, D. Xu, Flexible micro thermoelectric generators with high power density and light weight, Nano Energy 105 (2023).
[21] A.B. Zhang, B.L. Wang, D.D. Pang, J.B. Chen, J. Wang, J.K. Du, Influence of leg geometry configuration and contact resistance on the performance of annular thermoelectric generators, Energ. Conver. Manage. 166 (2018) 337–342.
[22] R. Lamba, S.C. Kaushik, S.K. Tyagi, Geometric optimization of trapezoidal thermoelectric heat pump considering contact resistances through genetic algorithm, Int. J. Energy Res. 42 (2018) 633–647.
[23] S. Siouane, S. Jovanović, P. Poure, Fully electrical modeling of thermoelectric generators with contact thermal resistance under different operating conditions, J. Electron. Mater. 46 (2016) 40–50.
[24] A. Yusuf, N. Bayhan, A.A. Ibrahim, H. Tiryaki, S. Ballikaya, Geometric optimization of thermoelectric generator using genetic algorithm considering contact resistance and Thomson effect, Int. J. Energy Res. 45 (2021) 9382–9395.
[25] B. B, A.G. Kaushik Raam, S. V, N.M. C.M, A. Al-Durra, Investigation on arrangement of thermoelectric modules based on exhaust gas flow direction to minimize mismatch power loss in TEG arrays, Appl. Therm. Eng. 221 (2023) 119853.
[26] A. Mohammadi, O.A. Jianu, Novel thermoelectric generator heat exchanger for indirect heat recovery from molten CuCl in the thermochemical Cu–Cl cycle of hydrogen production, Int. J. Hydrogen Energy 48 (2023) 5001–5017.
[27] Y. Ji, S. Lv, Experimental and numerical investigation on a radiative cooling driving thermoelectric generator system, Energy 268 (2023) 126734.
[28] W. Yang, W. Zhu, Y. Li, C. Xie, B. Xiong, Y. Shi, W. Lin, Global structural optimization of annular thermoelectric generators based on a dual-finite-element multiphysical model, Appl. Therm. Eng. 220 (2023) 119797.
[29] D. Luo, Z. Wu, Y. Yan, D. Ji, Z. Cheng, R. Wang, Y. Li, X. Yang, Optimal design of a heat exchanger for automotive thermoelectric generator systems applied to a passenger car, Appl. Therm. Eng. 227 (2023) 120360.
[30] Z.-G. Shen, B. Huang, X. Liu, Effect of structure parameters on the performance of an annular thermoelectric generator for automobile exhaust heat recovery, Energ. Conver. Manage. 256 (2022).
[31] Y. Ge, K. He, L. Xiao, W. Yuan, S.-M. Huang, Geometric optimization for the thermoelectric generator with variable cross-section legs by coupling finite element method and optimization algorithm, Renew. Energy 183 (2022) 294–303.
[32] W. Yang, A. Xu, W. Zhu, Y. Li, Y. Shi, L. Huang, H. Li, W. Lin, C. Xie, Performance improvement and thermomechanical analysis of a novel asymmetrical annular thermoelectric generator, Appl. Therm. Eng. 237 (2024).
[33] Y. Sun, P. Zhai, S. Wang, B. Duan, G. Li, G. Chen, Performance enhancement of segmented annular thermoelectric generator based on multi-parameter and multi-objective optimization, Therm. Sci. Eng. Progress 47 (2024).
[34] Q. Tan, G. Chen, Y. Sun, B. Duan, G. Li, P. Zhai, Performance of annular thermoelectric couples by simultaneously considering interface layers and boundary conditions, Appl. Therm. Eng. 174 (2020) 115301.
[35] C.N. Kim, Development of a numerical method for the performance analysis of thermoelectric generators with thermal and electric contact resistance, Appl. Therm. Eng. 130 (2018) 408–417.

[36] H. He, Y. Wu, W. Liu, M. Rong, Z. Fang, X. Tang, Comprehensive modeling for geometric optimization of a thermoelectric generator module, Energ. Conver. Manage. 183 (2019) 645–659.
[37] H. Yao, W. Pu, J. Wang, Y. Qin, L. Qiao, N. Song, A novel thermosyphon cooling applied to concentrated photovoltaic-thermoelectric system for passive and efficient heat dissipation, Appl. Therm. Eng. 236 (2024).
[38] S. Wang, T. Xie, H. Xie, Experimental study of the effects of the thermal contact resistance on the performance of thermoelectric generator, Appl. Therm. Eng. 130 (2018) 847–853.
[39] J. Zhao, Z. Kuang, R. Long, Z. Liu, W. Liu, Impacts of thermal and electric contact resistance on the material design in segmented thermoelectric generators, Energy Storage Saving 3 (2024) 5–15.
[40] Y. Li, W. Zhu, D. Luo, Y. Shi, Y. Ren, X. Wang, Y. Yan, Experimental study on thermal contact resistance of thermoelectric generators, in: 3rd International Conference on Energy and Power, AIP Publishing, Thailand, 2021.
[41] Y. Li, Y. Shi, X. Wang, D. Luo, Y. Yan, Thermal and electrical contact resistances of thermoelectric generator: experimental study and artificial neural network modelling, Appl. Therm. Eng. 225 (2023) 120154.
[42] A.B. Zhang, B.L. Wang, D.D. Pang, L.W. He, J. Lou, J. Wang, J.K. Du, Effects of interface layers on the performance of annular thermoelectric generators, Energy 147 (2018) 612–620.
[43] R. Bjørk, The universal influence of contact resistance on the efficiency of a thermoelectric generator, J. Electron. Mater. 44 (2015) 2869–2876.
[44] A. Zhang, D. Pang, J. Lou, J. Wang, W.M. Huang, An analytical model for wearable thermoelectric generators harvesting body heat: an opportunistic approach, Appl. Therm. Eng. 236 (2024).
[45] Y. Zhu, D.W. Newbrook, P. Dai, C.H.K. de Groot, R. Huang, Artificial neural network enabled accurate geometrical design and optimisation of thermoelectric generator, Appl. Energy 305 (2022).
[46] K. Pietrzyk, B. Ohara, T. Watson, M. Gee, D. Avalos, H. Lee, Thermoelectric module design strategy for solid-state refrigeration, Energy 114 (2016) 823–832.
[47] S. Shittu, G. Li, X. Zhao, X. Ma, Y.G. Akhlaghi, E. Ayodele, Optimized high performance thermoelectric generator with combined segmented and asymmetrical legs under pulsed heat input power, J. Power Sources 428 (2019) 53–66.
[48] Z. Ouyang, D. Li, Modelling of segmented high-performance thermoelectric generators with effects of thermal radiation, electrical and thermal contact resistances, Sci. Rep. 6 (2016) 24123.